

A Second-Order Positivity-Preserving Finite Volume Upwind Scheme for Air-Mixed Droplet Flow in Atmospheric Icing

S. K. Jung* and R. S. Myong[†]

*Research and Development Division, Korea Aerospace Industries LTD., Sacheon, Gyeongnam,
664-942, South Korea

[†]Department of Aerospace and System Engineering and Research Center for Aircraft Parts
Technology, Gyeongsang National University, Jinju, Gyeongnam 660-701, South Korea

myong@gnu.ac.kr

Abstract: A second-order positivity-preserving finite volume upwind scheme based on the approximate Riemann solver is developed for computing the Eulerian two-phase flow composed of air and small water droplets in atmospheric icing. In order to circumvent a numerical problem due to the non-strictly hyperbolic nature of the original Eulerian droplet equations, a simple technique based on splitting of the original system into the well-posed hyperbolic part and the source term is proposed. The positivity-preserving Harten-Lax-van Leer-Contact approximate Riemann solver is then applied to the well-posed hyperbolic part of the Eulerian droplet equations. It is demonstrated that the new scheme satisfies the positivity condition for the liquid water contents. The numerical results of one and two-dimensional test problems are also presented as the verification and validation of the new scheme. Lastly, the exact analytical Riemann solutions of the well-posed hyperbolic part of the droplet equations in wet and dry regions are given for the verification study.

Keywords: CFD, two-phase flow, Eulerian, approximate Riemann solver

1 Introduction

Two-phase flows are very common in many scientific and engineering applications ranging from fluid dynamics, chemical engineering, combustion and many more. Accurate mathematical and computational modeling of these two-phase flow phenomena is currently a very active field of research. For example, Toumi and Kumbaro [1] developed an approximate linearized Riemann solver for the numerical simulation of an isentropic two-component two-phase flow. Saurel and Abgrall [2] also proposed a new isentropic two-phase model and an associated Godunov method for compressible multi-fluid and multi-phase flows. It was later recognized by Tian *et al.* [3] that the compressible two-phase model equations cannot always be written in conservative form, though they may be hyperbolic. In order to resolve this problem, they developed a path-conservative method for a five-equation model of two-phase flow with an approximate Harten-Lax-van Leer-Contact(HLLC)-type Riemann solver. In these works, two-phase flows are treated in a strongly coupled manner so that the equations of each phase are fully solved and thus both phases (gas and liquid) affect each other strongly, even though no viscous effects are assumed to be present in the physical system.

There is a very important two-phase flow in which a drastic physical simplification is possible. Such a case is found in the air-mixed droplet flow field that describes the gas-liquid two-phase diluted flows around aircraft flying inside a cloud composed of compressible air and small super-cooled droplets of liquid water in the atmosphere. This is called *atmospheric in-flight icing* in the field and remains as a critical technological issue in the safety of aircraft [4-6]. A similar problem can be found in wind turbine blades operating in cold climate. It is called simply *atmospheric icing* in the field [7]. The two-phase flow in those situations can be simulated using a weakly coupled (or one-way coupling) algorithm since the effects of a droplet on the air flow can be ignored. In general, the mass loading ratio of the bulk density of the droplets over the bulk

density of air is on the order of 10^{-3} under icing conditions. This observation can therefore justify a weakly coupled algorithm in which separate calculations are made of the atmosphere cloud condition mixed with the air and a super-cooled water droplet. Under this condition, the Eulerian droplet equations of two-phase flow can be written as [8,9]

$$\begin{aligned}\rho_t + \nabla \cdot (\rho \mathbf{u}) &= 0, \\ (\rho \mathbf{u})_t + \nabla \cdot (\rho \mathbf{u} \mathbf{u}) &= \mathbf{S}(\rho, \rho_g, T_g, \mathbf{u}, \mathbf{u}_g, \mathbf{g}).\end{aligned}\tag{1.1}$$

In these *convection-type* equations with no diffusion terms, the ρ and \mathbf{u} are the droplet density in terms of liquid water content (LWC) and the velocity of the droplet, respectively. The ρ_g , T_g , \mathbf{u}_g and \mathbf{g} are the air density, the air temperature, the air velocity, and the acceleration vector due to gravity, respectively. The vector \mathbf{S} represents the source effects which include the aerodynamic drag term, gravity term, and buoyancy term of the droplet. The effects of the air flow in the one-way coupling algorithm appear only through the source term.

There are at present two unsolved computational issues regarding this weakly coupled air-droplet model. The first issue concerns the accuracy of numerical solutions to the droplet equations (1.1). In particular, a very low density of droplets can be observed around a solid surface after the droplets impinge on the surface of a moving object such as flying aircraft. Without proper *positivity-preserving* schemes, the water droplet density near the surface may become negative, which is unphysical. Even worse, this numerical breakdown is not rare in case of air-mixed droplet flow and, as a consequence, it becomes one of the most critical issues in developing proper numerical schemes. However, owing to the difficulty to solve this rather tricky problem, most of previous computational codes on the Eulerian droplet equations have not been shown positivity-preserving and, instead, remain first-order in order to slow the appearance of breakdown [10]. To the best knowledge of the authors, no *second-order positivity-preserving finite volume upwind scheme for air-mixed droplet flow in in-flight and atmospheric icing* has

been reported in the literature. The positivity-preserving property is also closely related to the capability of numerical schemes in accurately resolving nonlinear wave regions: shock fronts, rarefactions, and contact discontinuities. It is well established that transitional layers exist at the interface of the shadow and non-shadow areas in the droplet fields and the accurate prediction of shadow boundaries around an aircraft plays a vital role in selecting the proper location of the ice detector.

The second unsolved computational issue is the need for a *unified solver* for the Eulerian droplet equations and the Navier-Stokes-Fourier equations of air flow. One of the main advantages of Eulerian over Lagrangian in the mathematical form of droplet equations is that exactly the same numerical scheme initially developed for the strictly hyperbolic conservation laws in the Navier-Stokes-Fourier equations of air flow and associated computational grid can be applied to numerical solutions of the droplet equations as well. This feature should not be underestimated since the droplet and air solvers are repeatedly used in the computational simulation of icing accretion which typically runs on the order of minutes. Therefore a unified solver can be considered a vital part of any efficient icing simulation code.

The Eulerian droplet equations (1.1) as they stand may, however, not be suitable for tackling the aforementioned computational issues. The reason is that the convective system of the Eulerian droplet equations, the left-hand side of the equations (1.1), is not strictly hyperbolic. Even though the system has real eigenvalues, $\lambda_{i=1,2,3}=u$, are not distinct, that is, degenerate. This means that the well-known methods based on the well-posed strictly hyperbolic system may not be applicable and the special scheme based on other concepts such as the kinetic approximation [11] is required.

In order to circumvent this problem, a new method based on a strategy developed originally in computational magnetohydrodynamics (MHD) is proposed in the present study. The idea can be traced to the eight-wave system of the upwind-type MHD schemes in which a vector term

involving the divergence of the magnetic field, $\mathbf{B}(\nabla \cdot \mathbf{B})$, is added and subtracted to the momentum equation for purely numerical purpose. The method was pioneered by Powell and Roe *et al.* [12,13] and has been used extensively in the computational MHD community [14]. By taking advantage of the idea, a vector term of similar spirit, $\nabla \cdot (\rho g d \mathbf{I})$ in the present problem, is added and subtracted to the left-hand side of the Eulerian droplet momentum equation (1.1):

$$\begin{bmatrix} \rho \\ \rho \mathbf{u} \end{bmatrix}_t + \nabla \cdot \begin{bmatrix} \rho \mathbf{u} \\ \rho \mathbf{u} \mathbf{u} + \rho g d \mathbf{I} - \rho g d \mathbf{I} \end{bmatrix} = \begin{bmatrix} 0 \\ \mathbf{S}(\rho, \rho_g, T_g, \mathbf{u}, \mathbf{u}_g, \mathbf{g}) \end{bmatrix}, \quad (1.2)$$

Equivalently in split form,

$$\begin{bmatrix} \rho \\ \rho \mathbf{u} \end{bmatrix}_t + \nabla \cdot \begin{bmatrix} \rho \mathbf{u} \\ \rho \mathbf{u} \mathbf{u} + \rho g d \mathbf{I} \end{bmatrix} - \begin{bmatrix} 0 \\ \nabla \cdot (\rho g d \mathbf{I}) \end{bmatrix} = \begin{bmatrix} 0 \\ \mathbf{S}(\rho, \rho_g, T_g, \mathbf{u}, \mathbf{u}_g, \mathbf{g}) \end{bmatrix},$$

where d represents a reference size of droplets.

Now the original not-strictly hyperbolic pressure-less system is divided into the well-posed hyperbolic part and a term of source nature. It should be noted that a similar splitting technique was also developed by Myong and Roe [15] in computational magnetohydrodynamics to define numerical flux based on the well-posed planar Riemann problem and the evolution of Alfvén waves. The choice of the specific form of the term $\nabla \cdot (\rho g d \mathbf{I}) = g d \nabla \cdot (\rho \mathbf{I})$ is motivated by the fact that the pressure term $\nabla \cdot (p \mathbf{I})$ disappears when the weakly coupled two-phase model (1.1) is derived from the strongly coupled two-phase model, such as the Saurel-Abgrall model [2]. After introducing an approximation $p \sim \rho$ and multiplying a constant $g d$ to make the dimension of term equal, the present choice is shown to be equivalent to the pressure term in principle. In this stage one might consider the liquid pressure term $\nabla \cdot (p \mathbf{I})$, instead of $g d \nabla \cdot (\rho \mathbf{I})$, but this will impose an unnecessary burden of deriving additional equation of state

for the droplet density ρ , let alone making the problem more complicated by losing sight of original pure numerical objective of the splitting technique. Then the first and second terms of the left-hand side of the system (1.2) are well-posed and consequently it can be easily treated within the computational framework of the approximate Riemann solver. On the other hand, the term subtracted to the left-hand side can be treated numerically as a simple source term. In passing, it should be emphasized that, *since the same term is added and subtracted, the resulting equation (1.2) is mathematically equivalent to the original equation (1.1)*. For this reason, all other aspects of the scheme, such as the numerical boundary conditions, remain exactly the same. The well-posed hyperbolic part of the model (1.2) will be designated as the shallow water type droplet equations (SWDEs) since it resembles the shallow water equations (SWEs) studied extensively in ocean and hydraulic engineering [16-19]. The SWDEs are almost identical to the SWEs, with an equivalence relation ρ (LWC of the droplet) $\leftrightarrow h$ (height of water), both of which are positive scalar.

Even though the SWDEs satisfies the strictly hyperbolic property, there still remains a question of whether the upwind-type schemes, to meet the positivity-preserving property, can be developed. In any in-flight and atmospheric icing code, the capability of computing the shadow area, defined as the region around the solid surface with very low droplet density, is essential. However, it is well-known that the positivity of numerical solutions of the Roe-type flux difference splitting scheme is not guaranteed. While the flux vector splitting schemes are known to be free from this drawback [20], any such scheme also suffers an intrinsic incompatibility between the desirable positivity-preserving property and the accurate resolution of contact discontinuities [21]. Einfeld *et al.* [22] introduced the class of positively conservative schemes that always generate non-negative density from physical data. They proved that the Godunov scheme is positively conservative, but no scheme whose interface flux derives from a linearized Riemann solution can be positively conservative. In addition, they showed that the Harten-Lax-

van Leer (HLLC) scheme [23] is positively conservative, provided the absolute values of the maximal and minimal wave speeds satisfy certain stability bounds. On the basis of these findings, Toro *et al.* [24] developed the so-called Harten-Lax-van Leer-Contact (HLLC) approximate Riemann solver, which restores the contact surface in the HLL-Riemann scheme, and applied it to the SWEs [16].

In this study the positivity-preserving HLLC scheme based on the characteristics decomposition is applied to the well-posed hyperbolic part of the model (1.2), that is, the SWDEs. It will be shown that this numerical scheme satisfies the density positivity condition and can serve as the basic building block for the second-order unified solver of air-mixed droplet flow over arbitrarily complex bodies or in internal passages. In Section 2 we review the mathematical model of the air-droplet two-phase flow and present the well-posed hyperbolic part of the Eulerian droplet equations. We also study the eigen-structure of the system as a foundation for the HLLC Riemann solver. In Section 3 we present the second-order finite volume method based on the HLLC approximate Riemann solver for the Eulerian droplet equations. In Section 4 we present numerical results of one and two-dimensional test problems as the verification and validation of the new scheme. Lastly, the exact analytical Riemann solutions of the well-posed hyperbolic part of the droplet equations in wet and dry regions are given in Appendices for the purpose of the verification study.

2 Governing equations of air-droplet two-phase flow

2.1 Compressible Navier-Stokes-Fourier equations for air flow

Prior to the simulation of the droplet flow fields, the air flow should be computed to provide the droplet solver with the air flow information, through the source term in the Eulerian droplet equations (1.1) or (1.2). The compressible Navier-Stokes-Fourier equations are employed for this

purpose:

$$\begin{bmatrix} \rho_g \\ \rho_g \mathbf{u}_g \\ E \end{bmatrix}_t + \nabla \cdot \begin{bmatrix} \rho_g \mathbf{u}_g \\ \rho_g \mathbf{u}_g \mathbf{u}_g + p \mathbf{I} \\ (E + p) \mathbf{u}_g \end{bmatrix} = \nabla \cdot \begin{bmatrix} 0 \\ \boldsymbol{\tau} \\ \boldsymbol{\tau} \cdot \mathbf{u}_g + \mathbf{Q} \end{bmatrix}, \quad (2.1)$$

where

$$\boldsymbol{\tau} = 2\mu [\nabla \mathbf{u}_g]^{(2)}, \quad \mathbf{Q} = k \nabla T.$$

Here ρ_g , \mathbf{u}_g , p , and E represent the density, the velocity, the pressure, and the total energy of the air, respectively. The non-conserved variables $\boldsymbol{\tau}$ and \mathbf{Q} denote the viscous shear stress tensor and the heat flux, respectively. The symbol $[\mathbf{A}]^{(2)}$ in the shear stress tensor stands for the traceless symmetric part of the tensor \mathbf{A} . The μ and k are the viscosity and thermal conductivity, respectively, and depend on the air temperature. For the air flow, the ideal equation of state $p = \rho_g RT$ is used.

2.2 Eulerian droplet equations

The basis of the Eulerian droplet equations is the treatment of the dispersed phase as a continuum. Since the mass loading of the bulk density of the droplets is negligible in in-flight icing, the weakly coupled two-phase model may be adopted. A number of phenomena and forces may be considered, but the following assumptions are sensible for in-flight icing situations: the droplets are spherical without deformation or breaking; there is no collision, coalescence or splashing of droplets; there is no heat or mass exchange between the droplets and the surrounding air; the turbulence effects on the droplets are negligible; and the only forces acting on the droplets are due to aerodynamic drag, gravity, and buoyancy.

The two-dimensional continuity and momentum equations of the droplets in the Eulerian form

(1.1) can be written as

$$\begin{bmatrix} \rho \\ \rho u \\ \rho v \end{bmatrix}_t + \begin{bmatrix} \rho u \\ \rho u^2 \\ \rho uv \end{bmatrix}_x + \begin{bmatrix} \rho v \\ \rho uv \\ \rho v^2 \end{bmatrix}_y = \mathbf{S}, \quad (2.2)$$

where the source term associated with air flow and the gravity and buoyancy of droplets is given by

$$\mathbf{S} = \begin{bmatrix} 0 \\ A_u(u_g - u) \\ A_v(v_g - v) + \rho g(1 - \rho_g/\rho_w) \end{bmatrix}.$$

The u and v are x and y directional velocities of the droplet, respectively. The $A_u(u_g - u)$ and $A_v(v_g - v)$ in the source term denote the drag caused by the air flow while the $\rho g(1 - \rho_g/\rho_w)$ denotes the resultant force of the gravity and buoyancy of droplets. The coefficients A_u and A_v are defined as

$$A_u = \frac{0.75 \cdot \rho \cdot C_{D_u} \cdot \text{Re}_u \cdot \mu}{\rho_w \cdot \text{MVD}^2}, \quad \text{Re}_u = \frac{\rho_g \cdot \text{MVD}}{\mu} |u_g - u|, \quad (2.3)$$

$$A_v = \frac{0.75 \cdot \rho \cdot C_{D_v} \cdot \text{Re}_v \cdot \mu}{\rho_w \cdot \text{MVD}^2}, \quad \text{Re}_v = \frac{\rho_g \cdot \text{MVD}}{\mu} |v_g - v|, \quad (2.4)$$

where Re_u and Re_v are the Reynolds number of the droplets, C_{D_u} and C_{D_v} are the drag coefficients of the spherical droplets, and MVD is the mean volume diameter of the droplet. By using Langmuir et al.'s results [25], the following expressions for the drag coefficients can be derived:

$$C_{D_u} = \frac{24}{\text{Re}_u} \left(1 + 0.0197 \text{Re}_u^{0.63} + 2.6 \cdot 10^{-4} \text{Re}_u^{1.38} \right), \quad (2.5)$$

$$C_{D_v} = \frac{24}{\text{Re}_v} \left(1 + 0.0197 \text{Re}_v^{0.63} + 2.6 \cdot 10^{-4} \text{Re}_v^{1.38} \right), \quad (2.6)$$

which are valid for Re_u and $\text{Re}_v < 1000$.

2.3 Convective part of the Eulerian droplet equations

Through simple checking of the eigenvalues of the system (2.2),

$$\begin{bmatrix} \rho \\ u \\ v \end{bmatrix}_t + \begin{bmatrix} u & \rho & 0 \\ 0 & u & 0 \\ 0 & 0 & u \end{bmatrix} \begin{bmatrix} \rho \\ u \\ v \end{bmatrix}_x = \begin{bmatrix} 0 \\ 0 \\ 0 \end{bmatrix},$$

it can be confirmed that the system is not well-posed. Instead, by adopting the splitting technique explained in (1.2) of the introduction section, the following well-posed hyperbolic part can be obtained:

$$\mathbf{U}_t + \mathbf{F}_x = \mathbf{0}, \quad (2.7)$$

where

$$\mathbf{U} = \begin{bmatrix} \rho \\ \rho u \\ \rho v \end{bmatrix}, \quad \mathbf{F} = \begin{bmatrix} \rho u \\ \rho u^2 + \rho g d \\ \rho u v \end{bmatrix}.$$

This system will be the basis for developing the positivity-preserving HLLC approximate Riemann solver for the Eulerian droplet equations.

3 Finite volume method based on the approximate Riemann solver

3.1 HLLC approximate Riemann solver for the well-posed hyperbolic part

For the well-posed hyperbolic part, the very low depth caused by the rarefaction waves is analogous to the shadow area, which refers to the very low density of the droplets around a solid surface after the droplets impinge on the solid surface. Fig. 1 illustrates the shadow and non-shadow areas around an airfoil. Although various numerical methods for the SWEs have been published in the past, only a few methods satisfy the depth positivity in a dry bed. In particular, the HLLC approximate Riemann solver developed by Toro *et al.* [24] has shown good behavior and satisfies the depth positivity. The HLLC scheme is a modification of the basic HLLE scheme; it accounts for the influence of the intermediate waves.

Fig. 2 clearly demonstrates the need of a positivity-preserving scheme for Eulerian droplet equations. The Roe solver breaks down completely near the solid wall of the airfoil where the negative-density generating rarefaction waves are formed. Owing to this numerical breakdown, most of previous codes on the Eulerian droplet equations remain first-order in order to slow the appearance of breakdown [10], which compromises the accuracy of numerical solutions like the collection efficiency on the solid surface.

Fig. 3 illustrates the assumed wave structure in the HLLC approximate Riemann solver. There are two distinct fluxes for the star region. In the exact Riemann solver, the middle wave speed S_* can be estimated for the particle velocity in the middle state ($S_*=u_*$). The structure of the HLLC scheme can be derived for the well-posed hyperbolic part of the droplet equations (2.7). The governing equations in one-dimensional case may be rewritten as follows with a change of notation $\psi=v$:

$$\begin{bmatrix} \rho \\ \rho u \\ \rho \psi \end{bmatrix}_t + \begin{bmatrix} \rho u \\ \rho u^2 + \rho g d \\ \rho u \psi \end{bmatrix}_x = \begin{bmatrix} 0 \\ 0 \\ 0 \end{bmatrix}. \quad (3.1)$$

The tangential velocity component $\psi(x, t)$ represents the concentration of a pollutant or some

other passive scalar. The quantity ψ gives rise to the middle eigenvalue, $\lambda_2=u$. For this hyperbolic system, the following HLLC flux may be defined at the interface of the left and right cells

$$A_{i+\frac{1}{2}} = \begin{cases} A_L & \text{if } 0 \leq S_L, \\ A_{*L} & \text{if } S_L \leq 0 \leq S_*, \\ A_{*R} & \text{if } S_* \leq 0 \leq S_R, \\ A_R & \text{if } 0 \geq S_R, \end{cases} \quad (3.2)$$

where

$$A_{*L} = A_L + S_L (U_{*L} - U_L), A_{*R} = A_R + S_R (U_{*R} - U_R).$$

The states, U_{*L} , U_{*R} , and the wave speed, S_L , S_R , are given by,

$$U_{*K} = \rho_k \begin{pmatrix} \frac{S_K - u_K}{S_K - S_*} \\ S_* \\ \psi_K \end{pmatrix}, \quad S_L = u_L - a_L q_L, \quad S_R = u_R + a_R q_R, \quad (3.3)$$

where $a_L=a_R=\sqrt{gd}$. In these expressions, the left and right wave speeds are determined by an eigenvalues-based minimum and maximum signal velocities proposed by Davis [26] on the basis of the Roe average [27,28]. On the other hand, the middle wave speed, S_* , can be determined by direct wave speed estimates using Rankine-Hugoniot conditions proposed by Toro [17]. In this study, the following direct wave speed estimate is employed to define the wave speed on the star region:

$$S_* = \frac{S_L \rho_R (u_R - S_R) - S_R \rho_L (u_L - S_L)}{\rho_R (u_R - S_R) - \rho_L (u_L - S_L)}, \quad (3.4)$$

which is obtained from manipulations of equations (3.1). This wave speed estimate for S_* has the remarkable property of being exact when one of the data states is a dry bed state. In equation (3.3), q_K is defined by

$$q_K = \begin{cases} \sqrt{\frac{\rho_*}{\rho_K}} & \text{if } \rho_* > \rho_K, \\ 1 & \text{if } \rho_* \leq \rho_K, \end{cases} \quad (3.5)$$

where ρ_* is an estimate of the exact solution for ρ in the star region. From the depth positivity condition, ρ_* and u_* for depth and particle velocity in the star region are derived as follows:

$$\rho_* = \frac{1}{2}(\rho_L + \rho_R) - \frac{1}{4}(u_R - u_L) \frac{\rho_L + \rho_R}{a_L + a_R}, \quad u_* = \frac{1}{2}(u_L + u_R) - \frac{1}{4}(\rho_R - \rho_L) \frac{a_L + a_R}{\rho_L + \rho_R}. \quad (3.6)$$

The third component of the flux can be expressed in terms of the first component and the variable ψ , that is $A^3 = A^1 \psi$, where A^3 is defined as follows:

$$A^3_{i+\frac{1}{2}} = \begin{cases} A^1_{i+\frac{1}{2}} \psi_L & \text{if } u_* \geq 0, \\ A^1_{i+\frac{1}{2}} \psi_R & \text{if } u_* \leq 0. \end{cases} \quad (3.7)$$

In order to enhance the accuracy, Monotone Upstream Scheme for Conservation Law (MUSCL) proposed by van Leer [29] together with van Albada limiter [30] is employed:

$$\mathbf{W}_R = \mathbf{W}_{i+1} - \frac{1}{2} \Psi_R (\mathbf{W}_{i+2} - \mathbf{W}_{i+1}), \quad \mathbf{W}_L = \mathbf{W}_i + \frac{1}{2} \Psi_L (\mathbf{W}_i - \mathbf{W}_{i-1}), \quad (3.8)$$

where $\mathbf{W} = [\rho, u, \psi]^T$ denotes primitive variables. The van Albada limiter is defined as

$$\Psi_{L/R} = \frac{1}{2} [(1 + \kappa) r_{L/R} + (1 - \kappa)] \Phi_{L/R}, \quad \Phi(r) = \frac{2r}{1 + r^2}, \quad (3.9)$$

where κ represents an extrapolation parameter and

$$r_R = \frac{\mathbf{W}_{i+1} - \mathbf{W}_i}{\mathbf{W}_{i+2} - \mathbf{W}_{i+1}}, \quad r_L = \frac{\mathbf{W}_{i+1} - \mathbf{W}_i}{\mathbf{W}_i - \mathbf{W}_{i-1}}.$$

A general procedure to precisely solve the Riemann problem for one-dimensional droplet equations (3.1) is summarized in Appendices A and B and Fig. 4. The star region values ρ^* and u^* can be determined using equations (A.1) to (A.3), and (A.4), respectively. The left and right rarefaction and shock waves can be determined using equations (A.9) and (A.12), and (A.5) and (A.10), respectively.

3.2 Two-dimensional finite volume formulation

The present finite volume formulation for the Eulerian droplet equations is based on a cell-centered scheme and structured grid. The complete set for the two-dimensional Eulerian droplet equations with the source terms can be written as

$$\frac{\partial}{\partial t} \int_{\Omega} \mathbf{U} d\Omega + \oint_{\partial\Omega} \mathbf{H} dl = \int_{\Omega} (\mathbf{S} + \mathbf{Q}) d\Omega, \quad (3.10)$$

where $\mathbf{H} = \mathbf{F} \cos\theta + \mathbf{G} \sin\theta$, and

$$\mathbf{U} = \begin{bmatrix} \rho \\ \rho u \\ \rho v \end{bmatrix}, \quad \mathbf{F} = \begin{bmatrix} \rho u \\ \rho u^2 + \rho g d \\ \rho uv \end{bmatrix}, \quad \mathbf{G} = \begin{bmatrix} \rho v \\ \rho uv \\ \rho v^2 + \rho g d \end{bmatrix},$$

$$\mathbf{S} = \begin{bmatrix} 0 \\ A_u (u_g - u) \\ A_v (v_g - v) + \rho g (1 - \rho_g / \rho_w) \end{bmatrix}, \quad \mathbf{Q} = g d \begin{bmatrix} 0 \\ \partial\rho / \partial x \\ \partial\rho / \partial y \end{bmatrix}.$$

Note that the subtracted term $gd\nabla \cdot (\rho\mathbf{I})$ in (1.2), denoted by \mathbf{Q} in (3.10), is moved from the left-hand side to the right-hand side for convenience. Here $\partial\Omega$ represents the bounding surface of the control volume Ω . The two-dimensional finite volume formulation in general non-Cartesian domains can be derived by exploiting the rotational invariance property of the Eulerian droplet equations, $\mathbf{F}(\mathbf{U})\cos\theta + \mathbf{G}(\mathbf{U})\sin\theta = T^{-1}\mathbf{F}(T\mathbf{U})$, where $T = T(\theta)$ represents the rotation matrix. The

equations (3.10) can then be expressed as

$$\frac{\partial \mathbf{U}}{\partial t} = -\frac{1}{\Omega} \left[\oint_{\partial \Omega} \mathbf{H} dl - \int_{\Omega} (\mathbf{S} + \mathbf{Q}) d\Omega \right]. \quad (3.11)$$

The line integral on the right-hand side can be approximated by a sum of the fluxes crossing the faces of the control volume. It is usually assumed that the flux is constant along the individual interface and is evaluated at the mid-point of the interface. Finally, we have the following discretized equation

$$\frac{d\mathbf{U}}{dt} = -\frac{1}{\Omega} \left[\sum_{k=1}^n \mathbf{H}_k \Delta l_k - \mathbf{S}\Omega - gd \sum_{k=1}^n \rho_k \begin{pmatrix} 0 \\ \mathbf{n}_k \end{pmatrix} \Delta l_k \right]. \quad (3.12)$$

The value of density at the interface is determined as follows

$$\rho_k = \begin{cases} \rho_L & \text{if } 0 \leq S_L, \\ \rho_{*L} & \text{if } S_L \leq 0 \leq S_*, \\ \rho_{*R} & \text{if } S_* \leq 0 \leq S_R, \\ \rho_R & \text{if } 0 \geq S_R. \end{cases} \quad (3.13)$$

In equation (3.12), the numerical flux \mathbf{H}_k at k -th interface is determined by the HLLC approximate Riemann solver. Although the implementation of explicit schemes is much easier than that of implicit schemes, explicit schemes require careful time step selection in order to fulfill the stability requirement. The droplet flow fields in this study are calculated under the maximum allowable time steps used in the work of Erduran *et al.* [19]. The local time stepping is achieved using the fifth stage Runge-Kutta scheme.

The collection efficiency, a main feature in in-flight and atmospheric icing, is determined using the density and velocity fields near the solid surface. Therefore, the setting of the solid surface condition is an important factor in solving droplet flow fields. In present study, a conventional

boundary condition used in the previous works [5-7,10] is employed. When the projection of a normal vector on a solid surface and the droplet velocity in an adjacent cell on the solid surface is positive, the droplets should not collide with the solid surface. This behaviour leads to a boundary condition on the solid surface following the sign of the projection as follows (see Fig. 5):

$$\begin{aligned} \mathbf{U}_{wall} &= 0 & \text{if } \mathbf{V} \cdot \mathbf{n} \geq 0, \\ \mathbf{U}_{wall} &= \mathbf{U} & \text{if } \mathbf{V} \cdot \mathbf{n} \leq 0, \end{aligned} \quad (3.14)$$

where $\mathbf{n}=(n_x, n_y)$ denotes the normal vector on the surface. For the inflow and outflow, the values of all eigenvalues turn out to have the same sign in the problem considered in the present study. In passing, it must be noted that the term $(\mathbf{H}_k - g d \rho_k [0, \mathbf{n}_k]^T)$ in the final scheme (3.12), which is obtained by summing up the numerical flux again after the splitting through the well-posed hyperbolic part and the source term, retains the eigenvalues of the original droplet equations, meaning that the same boundary conditions are applicable. Therefore, the conservative variables on the boundary can be determined solely by the free-stream values.

4 Verification and Validation

Two types of problems are selected to validate the second-order positivity-preserving finite volume upwind scheme of Eulerian droplet equations for air-mixed droplet flow. The first problem is intended to compare the exact analytical and numerical solutions as a *verification* study. The second problem is the air-mixed droplet flow around an airfoil taken from Papadakis *et al.* [31] as a *validation* study. The conditions of the problems are summarized in Tables 1 and 2.

The exact and numerical solutions to the one-dimensional well-posed hyperbolic part of the droplet equations without pollutants are compared in Figs. 6 and 7. The computational domain size 50 and one hundred grid points with the CFL number 0.2 are used in these computations. It can be shown in Fig. 6 that the HLLC scheme indeed satisfies the density positivity condition; the

density remaining very low but always positive in the (dry) region between two identical rarefaction waves traveling in opposite directions. Furthermore, by recalling Fig. 1 of identification of the Riemann problem, it may be argued that the shadow boundary formed around an airfoil is nothing but the strong rarefaction waves found in the present Riemann problem. Also, the analogy between the Riemann problem of the well-posed hyperbolic part of the droplet equations and the density distribution of droplets around an airfoil may explain why the Roe flux difference splitting scheme breaks down first near the lower and rear solid wall of the airfoil—since the region is the center of the severe dry bed, which is most vulnerable to the negative density. The new scheme is, in general, found to be very accurate including resolving rarefaction waves. The gap in the particle velocity is, nonetheless, found in the vicinity of the very low density. The numerical reason behind this shortcoming for the HLLC scheme is well understood [17] and under the more pressing need of the positivity property the issue is left for future study. On the other hand, if the Roe's approximate Riemann solver is applied, the unphysical negative density appears from the center of the dry region.

Another Riemann problem (case 2) and its solutions are illustrated in Fig. 7. The case is considered in order to investigate the evolution of nonlinear waves after the collision of two streams, which represents the local high LWC (wet) region near the stagnation point around an airfoil where droplets of the free stream collide with the solid wall surface. It is clearly shown in Fig. 7 that the density increases drastically in the star region, indicating a local high LWC region. The new scheme for this wet case is found to be very accurate in predicting the shock location and resolving the shock discontinuities.

In order to validate the new scheme for droplet impingements in in-flight and atmospheric icing, experimental test cases are selected from the literature [31]. The following collection efficiency represents the droplet impingement intensity measured in the experiment:

$$\beta = \frac{\rho V}{\rho_\infty V_\infty},$$

where the velocity magnitude V is determined by a scalar product $(un_x + vn_y)$. This parameter plays a critical role in controlling the ice accretion on the surface. The experimental test was conducted in the test section of the NASA icing research tunnel. A CCD camera and laser system were used to measure the droplet impingement on NACA 65₂415 and GLC 305 airfoils.

The air flow should be computed prior to the simulation of droplet flow fields in the case of the weakly coupled algorithm. The compressible Navier-Stokes-Fourier equations (2.1) are employed as the governing equations. The air flow solver is based on a second-order upwind-type finite volume scheme with the Roe's approximate Riemann solver. The Green-Gauss approach is employed for evaluating the spatial gradient in viscous flux. The Spalart-Allmaras turbulent model is employed to simulate the turbulent effect in flow fields, since the effects of different turbulent models on the qualitative aspect of the collection efficiency are shown negligible. The fifth order Runge-Kutta explicit time marching is used for the temporal discretization. For the boundary conditions, non-slip and Riemann invariant conditions are applied to the solid surface and the far-fields, respectively. An ideal gas equation is used to close the system of equations. A structured grid with a C-type topology and a size of 421×65 and an equivalent unstructured triangular grid are used.

The Mach number and Reynolds number considered in this validation flow problem are 0.23 and 4.9×10^6 , respectively. A dilute case with 0.05 g/m^3 (MVD $11.5 \text{ }\mu\text{m}$) and a dense case with 0.19 g/m^3 (MVD $21.0 \text{ }\mu\text{m}$) are considered. The MVD values are assumed to have a mono-disperse distribution instead of a Langmuir distribution. A numerical simulation based on the new second-order positivity-preserving scheme is conducted with exactly the same structured and unstructured grids employed in the air solver. Figs. 8 and 9 show the collection efficiencies on the

NACA 64₂415 and GLC 305 airfoils, respectively. Here only results of the structured grid are shown, since the effects of grid types on the collection efficiency are shown small. The experimental, present computational, and LEWICE results are compared for angles of attack of 0°, 6°, and 8°. Even though there are some deviations in the peak collection efficiency, the present computational results are in close agreement with experimental data in both airfoils. Interestingly, better agreements are found for high LWC cases and in the upper surface part of the airfoil. Fig. 10 shows the LWC distributions around the airfoils and the shadow areas formed mainly in the upper part of the airfoils. Lastly, in order to investigate the droplet impingement behavior in flows involving flow separation, a higher angle of attack case was analyzed with the present method. As shown in Fig. 11, the massively separated region and associated droplet trajectories are well captured, confirming the capability of the present droplet code to handle the separated flow.

5 Concluding Remarks

A second-order positivity-preserving finite volume upwind scheme to circumvent the non-strictly hyperbolic nature of the original Eulerian droplet equations of the weakly coupled two-phase flow model, which severely limits the application of well-established upwind schemes based on the characteristic decomposition such as the Roe's approximate Riemann solver, is proposed. We believe it is a significant contribution since it resolves one of the major stumble blocks for developing the robust droplet code in in-flight and atmospheric icing. Without proper positivity-preserving treatment, the droplet codes not only suffer the complete breakdown due to the negative density but cannot also be extended to the second-order accuracy. It must be also noted that the breakdown in case of air-mixed droplet flow is not rare and is observed in virtually every airfoil type flows, while the breakdown in ordinary gas flow occurs only in very rare cases involving two strong rarefaction waves moving in opposite directions.

In the present study, the second-order positivity-preserving property is achieved by *splitting the non-strictly hyperbolic part of the Eulerian droplet equations into the well-posed hyperbolic part and the source term*. Indeed, by computing the verification and validation flow problems, it is demonstrated that the new scheme based on the split system satisfies the positivity property in the droplet density. During the process, two Riemann problems (dry and wet) are also identified to describe two dominant mechanisms (shadow area and high LWC area near the stagnation region) responsible for the generic pattern in the LWC distributions around an airfoil.

Even though the HLLC approximate Riemann solver is used as the basis for developing a positivity-preserving scheme in the present study, other positivity-preserving numerical methods may be applicable as well. Notable are recent methods [32,33] that are based on the simple flux limiter by combining the high-order numerical flux with the first-order Lax–Friedrichs flux to satisfy a sufficient condition for preserving positivity. Also, question of relatively large numerical dissipation of the HLLC scheme is considered less important than the critical issue of positivity-preserving. More importantly, it must be reiterated that the present method retains the same governing equations and thus it should not be misunderstood as a modification of governing equations. The differences, if there exist any, between the original non-strictly hyperbolic system and the split system consisting of the well-posed hyperbolic part and the source term, are of pure numerical nature and will appear only in the truncation error level. Also, it should be noted that question of the physical validity of the well-posed hyperbolic part is irrelevant to the present study, since it, just like the conventional shallow water equations, is mathematically well-posed and the well-posedness is the only question needed to answer for the numerical purpose.

The present study is confined to the droplet impingement problem in which droplets are assumed to be a rigid sphere. In the future, the new scheme will be extended to compute the super-cooled large droplet flow fields involving the deformation, break, spread and rebound of droplets.

Acknowledgements

This work was supported by the National Research Foundation of Korea funded by the Ministry of Education, Science and Technology (Priority Research Centers Program NRF 2012-048078 and Basic Science Research Program 2012-R1A1A4A01-010242), South Korea.

Appendix A: Exact Riemann Solution of the Well-Posed Hyperbolic Part in Wet Region

The Riemann problem of two variables ρ and u for the one-dimensional well-posed hyperbolic part (3.1) can be written as

$$\begin{bmatrix} \rho \\ \rho u \end{bmatrix}_t + \begin{bmatrix} \rho u \\ \rho u^2 + \rho g d \end{bmatrix}_x = 0. \quad (\text{A.1})$$

The solution ρ_* of the Riemann problem may be determined by solving an implicit algebraic equation

$$f(\rho) = f_L(\rho, \rho_L) + f_R(\rho, \rho_R) + \Delta u = 0, \quad \Delta u \equiv u_R - u_L, \quad (\text{A.2})$$

where the functions f_L and f_R are expressed as

$$f_L = \begin{cases} \sqrt{gd} \ln \left(\frac{\rho_*}{\rho_L} \right) & \text{if } \rho_* \leq \rho_L \quad (\text{rarefaction}), \\ (\rho_* - \rho_L) \sqrt{\left(\frac{gd}{\rho_* \rho_L} \right)} & \text{if } \rho_* > \rho_L \quad (\text{shock}), \end{cases} \quad (\text{A.3})$$

$$f_R = \begin{cases} \sqrt{gd} \ln \left(\frac{\rho_*}{\rho_R} \right) & \text{if } \rho_* \leq \rho_R \quad (\text{rarefaction}), \\ (\rho_* - \rho_R) \sqrt{\left(\frac{gd}{\rho_* \rho_R} \right)} & \text{if } \rho_* > \rho_R \quad (\text{shock}). \end{cases}$$

The solution of the particle velocity u_* in the star region follows:

$$u_* = \frac{1}{2}(u_L + u_R) + \frac{1}{2}[f_R(\rho_*, \rho_R) - f_L(\rho_*, \rho_L)]. \quad (\text{A.4})$$

For the unknown ρ_* in the star region, the Newton-Raphson iteration method can be used. The type of the left and right waves (shocks or rarefactions) can be determined by comparing the known ρ_* from equations (A.2-A.4) with ρ_L and ρ_R . When $\rho_* > \rho_L$, the left wave is a shock wave and its speed can be determined by using the Rankine-Hugoniot condition. By introducing the celerity $a_L = \sqrt{gd}$, the shock speed can be written as

$$S_L = u_L - a_L q_L, \quad q_L = \sqrt{\frac{\rho_*}{\rho_L}}. \quad (\text{A.5})$$

When $\rho_* \leq \rho_L$, the left wave becomes a rarefaction wave. The speeds of the head and the tail of the rarefaction wave are given, respectively,

$$S_{head} = u_L - a_L, \quad S_{tail} = u_* - a_*. \quad (\text{A.6})$$

The solution inside the left rarefaction wave may be written as

$$u - a = \frac{dx}{dt} = \frac{\hat{x}}{\hat{t}}. \quad (\text{A.7})$$

The generalized Riemann invariant of the left rarefaction wave is given as

$$u + a = u_L + a_L. \quad (\text{A.8})$$

Finally, the solutions u and a within the left rarefaction wave can be calculated by combining equations (A.7) and (A.8) as follows

$$u = \frac{1}{2} \left(u_L + a_L + \frac{\hat{x}}{\hat{t}} \right), \quad a = \frac{1}{2} \left(u_L + a_L - \frac{\hat{x}}{\hat{t}} \right). \quad (\text{A.9})$$

Similarly, the solution of the right wave may be obtained by considering a shock wave and a rarefaction wave. When $\rho_* > \rho_R$, the right wave is a shock wave with the speed

$$S_R = u_R + a_R q_R, \quad q_R = \sqrt{\frac{\rho_*}{\rho_R}}, \quad (\text{A.10})$$

where the celerity is defined as $a_R = \sqrt{gd}$. When $\rho_* \leq \rho_R$, the right wave is a rarefaction wave and its head and tail speeds are

$$S_{head} = u_R + a_R, \quad S_{tail} = u_* + a_*. \quad (\text{A.11})$$

The analytical solutions u and a within the left rarefaction wave become

$$u = \frac{1}{2} \left(u_R - a_R + \frac{\hat{x}}{\hat{t}} \right), \quad a = \frac{1}{2} \left(-u_R + a_R + \frac{\hat{x}}{\hat{t}} \right). \quad (\text{A.12})$$

Appendix B: Exact Riemann Solution of the Well-Posed Hyperbolic Part in Dry Region

The particle velocity in the dry regions where the density is zero by definition may be chosen arbitrary; for example, zero particle velocity. This choice, however, may cause a discontinuity jump in the particle velocity which might contribute to numerical difficulties in capturing this feature by numerical means. The dry region of the well-posed hyperbolic part of the droplet equations can be considered for three cases; single left rarefaction wave, single right rarefaction wave, and the middle between two rarefaction waves (Figs. 3 and 4). The first case (Fig. 4 left) is when the dry region is located on the right side. The solution consists of a single left rarefaction

wave associated with the left eigenvalue $\lambda_1=u-a$. A contact discontinuity of speed S_{*L} coincides with the tail of the rarefaction wave. Along the contact discontinuity, $\rho_*=0$ and, thus, $a=0$. The speed of the contact discontinuity can be derived by using equation (A.8),

$$S_{*L} = u_L + a_L. \quad (\text{B.1})$$

The complete solution can be expressed in terms of non-conserved variables (a, u)

$$(a, u)(x, t) = \begin{cases} (a, u)_L & \text{if } x/t \leq u_L - a_L, \\ (a, u)_{fan} & \text{if } u_L - a_L \leq x/t \leq S_{*L}, \\ (a, u)_0 & \text{if } S_{*L} \leq x/t, \end{cases} \quad (\text{B.2})$$

where

$$u_{fan} = \frac{1}{2} \left(u_L + a_L + \frac{\hat{x}}{\hat{t}} \right), \quad a_{fan} = \frac{1}{2} \left(u_L + a_L - \frac{\hat{x}}{\hat{t}} \right). \quad (\text{B.3})$$

The second case (Fig. 4 right) is when the dry region is located on the left side. The solution consists of a right rarefaction wave associated with $\lambda_2=u+a$. A contact discontinuity with the speed S_{*R} is given by

$$S_{*R} = u_R - a_R, \quad (\text{B.4})$$

and the complete solution is

$$(a, u)(x, t) = \begin{cases} (a, u)_0 & \text{if } x/t \leq S_{*R}, \\ (a, u)_{fan} & \text{if } S_{*R} \leq x/t \leq u_R + a_R, \\ (a, u)_R & \text{if } u_R + a_R \leq x/t, \end{cases} \quad (\text{B.5})$$

where

$$u_{fan} = \frac{1}{2} \left(u_R - a_R + \frac{\hat{x}}{\hat{t}} \right), \quad a_{fan} = \frac{1}{2} \left(-u_R + a_R + \frac{\hat{x}}{\hat{t}} \right). \quad (\text{B.6})$$

The last case (Fig. 4 middle) is when two rarefaction waves interact with different directions. The left and right rarefaction waves are associated with the eigenvalues $\lambda_1=u-a$ and $\lambda_2=u+a$, respectively. The dry region appears between the two rarefaction waves and the solution can be written by utilizing the solutions of the previous two cases as follows:

$$(a, u)(x, t) = \begin{cases} (a, u)_L & \text{if } x/t \leq S_{*L}, \\ 0 & \text{if } S_{*L} \leq x/t \leq S_{*R}, \\ (a, u)_R & \text{if } S_{*R} \leq x/t, \end{cases} \quad (\text{B.7})$$

where $(a, u)_L$ and $(a, u)_R$ are given by equations (B.2) and (B.5), respectively.

References

- [1] Toumi, I., and Kumbaro, A. (1996). An approximate linearized Riemann solver for a two-fluid model. *J. Comp. Phys.* 124, 286-300.
- [2] Saurel, R. and Abgrall, R. (1999). A multiphase Godunov method for compressible multifluid and multiphase flows. *J. Comp. Phys.* 150, 425-467.
- [3] Tian, B., Toro, E.F. and Castro, C.E. (2011). A path-conservative method for a five-equation model of two-phase flow with an HLLC-type Riemann solver. *Comp. Fluids* 46, 122-132.
- [4] Cebeci, T., and Kafyke, F. (2003). Aircraft icing. *Annual Review of Fluid Mechanics* 35, 11-21.
- [5] Pueyo, A., Brette, C., Vafa, S., and Akel, I. (2007). A comparison exercise of ice accretion simulations with 2D and 3D solvers. *SAE-2007-01-3338*.

- [6] Jung, S.K., Myong, R.S., and Cho, T.H. (2011). Development of Eulerian droplets impingement model using HLLC Riemann solver and POD-based reduced order method. *AIAA 2011-3907*.
- [7] Virk, M.S., Homola, M.C., and Nicklasson, P.J. (2010). Effect of rime ice accretion on aerodynamic characteristics of wind turbine blade profiles. *Wind Eng.* 34-2, 207-218.
- [8] Durst, F., Milojevic, M., and Schonung, B. (1984). Eulerian and Lagrangian predictions of particulate two-phase flows: A numerical study. *Applied Math. Modeling* 8, 101-115.
- [9] Scott, J., Hankey, W., Giessler, F., and Giolda, T. (1988). Navier–Stokes solution to the flow field over ice accretion shapes. *J. Aircraft* 25, 710-716.
- [10] Kim, J.W., Dennis, P.G., Sankar, L.N., and Kreeger, R.E. (2013). Ice accretion modeling using an Eulerian approach for droplet impingement. *AIAA Paper 2013-0246*.
- [11] Bouchut, F., Jin, S., and Li, X. (2003). Numerical approximations of pressureless and isothermal gas dynamics. *SIAM J. Num. Anal.* 41, 135-158.
- [12] Powell, K.G., Roe, P.L., Myong, R.S., Gombosi, T., and DeZeeuw, D.L. (1995). An upwind scheme for magnetohydrodynamics. *AIAA Paper 1995-1704*.
- [13] Powell, K.G., Roe, P.L., Linde, T.J., Gombosi, T.I., and de Zeeuw, D.L. (1999). A solution-adaptive upwind scheme for ideal magnetohydrodynamics. *J. Comp. Phys.* 154(2), 284-309.
- [14] Janhunen, P. (2000). A positive conservative method for magnetohydrodynamics based on HLL and Roe methods. *J. Comp. Phys.* 160, 649-661.
- [15] Myong, R.S., and Roe, P.L. (1998). On Godunov-type schemes for

- magnetohydrodynamics. part 1. a model system. *J. Comp. Phys.* 147(2), 545-567.
- [16] Dodd, N. (1998). A numerical model of wave run-up, overtopping and regeneration. *J. Water Port, Coast and Ocean Eng.* 124 (2), 73-91.
- [17] Toro, E.F. (2001). *Shock-capturing methods for free-surface shallow flows*. Wiley.
- [18] Xu, K. (2002). A well-balanced gas-kinetic scheme for the shallow water equations with source terms. *J. Comp. Phys.* 178-2, 533-562.
- [19] Erduran, K.S., Kutija, V., and Hewett, C.J.M. (2002). Performance of finite volume solutions to the shallow water equations with shock-capturing schemes. *Int. J. Numer. Meth. Fluids* 40 (10), 1237-1273.
- [20] Estivalezes, J.L., and Villedieu, P. (1996). High-order positivity-preserving kinetic schemes for the compressible Euler equations. *SIAM J. Numer. Anal.* 33(5), 2050-2067.
- [21] Gressier, J., Villedieu, P., and Moschetta, J.M. (1999). Positivity of flux vector splitting schemes. *J. Comp. Phys.* 155, 199-220.
- [22] Einfeldt, B., Munz, C.D., Roe, P.L., and Sjogreen, B. (1991). On Godunov-type methods near low densities. *J. Comp. Phys.* 92, 273-295.
- [23] Harten, A., Lax, P.D., and van Leer, B. (1983). On upstream differencing and Godunov-type schemes for hyperbolic conservation laws. *SIAM Review* 25 (1), 35-61.
- [24] Toro, E.F., Spruce, M., and Speares, W. (1994). Restoration of the contact surface in the HLL-Riemann solver. *Shock Waves* 4 (1), 25-34.
- [25] Langmuir, I., and Blodgett, K.B. (1946). A mathematical investigation of water droplet trajectories. *US Army Air Forces Tech. Rep.* 5418.

- [26] Davis, S.F. (1988). Simplified second-order Godunov-type methods. *SIAM J. Sci. Stat. Comput.* 9, 445-473.
- [27] Roe, P.L. (1981). Approximate Riemann solvers, parameter vectors, and difference schemes. *J. Comp. Phys.* 43, 357-372.
- [28] Einfeldt, B. (1988). On Godunov-type methods for gas dynamics. *SIAM J. Numer. Anal.* 25(2), 294-318.
- [29] van Leer, B. (1979). Towards the ultimate conservative difference scheme V. A second order sequel to Godunov's method. *J. Comp. Phys.* 32 (1), 101-136.
- [30] van Albada, G.D., van Leer, B., and Roberts, Jr, W.W. (1982). A comparative study of computational methods in cosmic gas dynamics. *Astronomy and Astrophysics* 108, 76-84.
- [31] Papadakis, M., Hung, K.E., Vu, G.T., Yeong, H.W., Bidwell, C.S., Breer, M.D., and Bencic, T.J. (2002). Experimental investigation of water droplet impingement on airfoils, finite wings, and an S-duct engine inlet. *NASA/TM-2002-211700*.
- [32] Hu, X.Y., Adams, N.A., and Shu, C.W. (2013). Positivity-preserving method for high-order conservative schemes solving compressible Euler equations. *J. Comp. Phys.* 242, 169-180.
- [33] Zhang, X., and Shu, C.W. (2010). On positivity preserving high order discontinuous Galerkin schemes for compressible Euler equations on rectangular meshes. *J. Comput. Phys.* 229, 8918-8934.

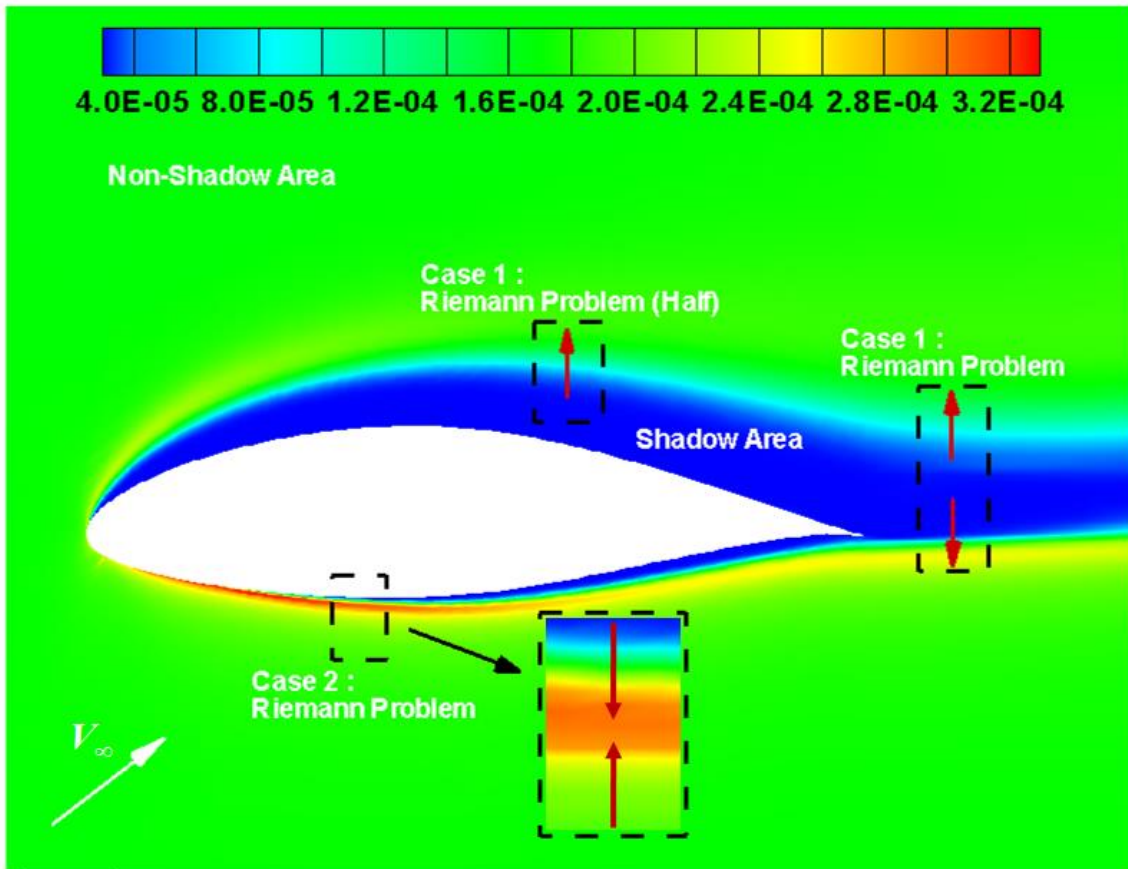


Fig. 1. Liquid water contents distribution around an airfoil and identification of the Riemann problem.

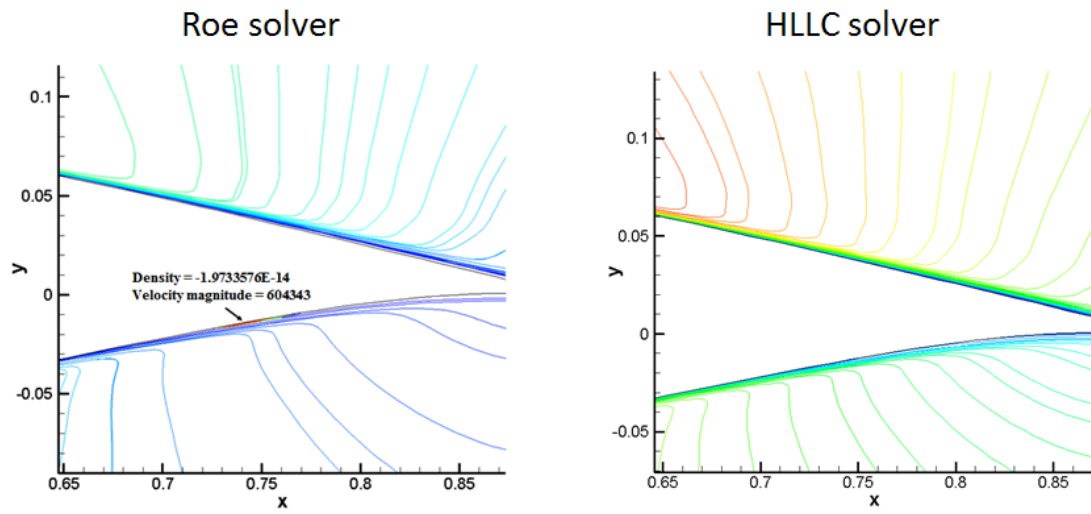


Fig. 2. Negativity droplet density breakdown of Roe solver in the Eulerian droplet equations and its cure by developing a second-order positivity-preserving HLLC solver of Eulerian droplet equations.

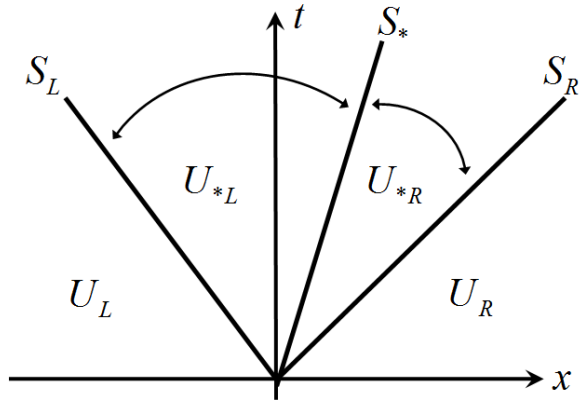


Fig. 3. The HLLC approximate Riemann solver for the well-posed hyperbolic part of the droplet equations.

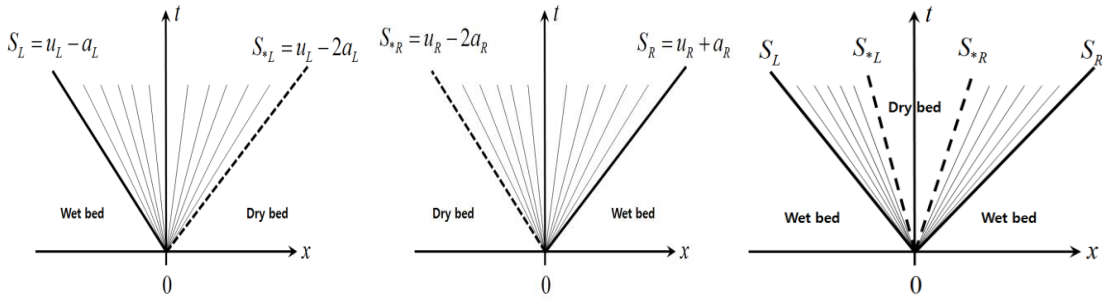


Fig. 4. Three cases in which the solution of the Riemann problem involves a dry region: (left) the dry region on the right; (right) the dry region on the left; (middle) the dry region between two wet regions.

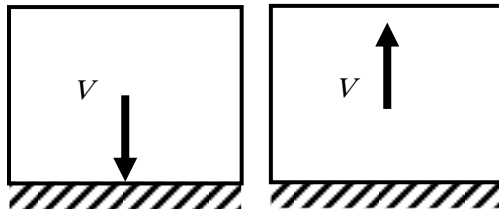


Fig. 5. Permeable wall boundary condition for droplet impingement.

Test cases	ρ_L	u_L	ρ_R	u_R	x_0	t
1	1.0	-5.0	1.0	5.0	25.0	2.5
2	1.0	5.0	0.1	-3.0	25.0	2.5

Table I. The verification case where x_0 and t represent the position of the initial discontinuity and the output time in seconds, respectively.

Airfoil model	MVD (μm)	LWC (g/m^3)	V_∞ (m/s)	c (m)	Re($\times 10^6$)
NACA 65 ₂ 415	11.5	0.05	78.7	0.928	4.85
	21	0.19			
GLC 305	11.5	0.05	78.7	0.914	4.83
	21	0.19			

Table II. The validation case: experimental conditions for airfoil test problems.

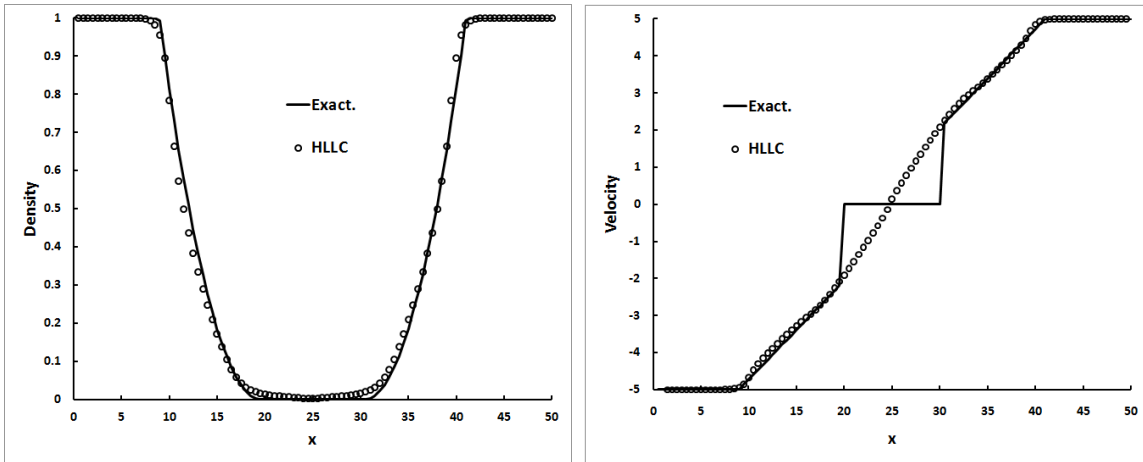


Fig. 6. The HLLC and the exact solutions of the density and velocity (test case 1).

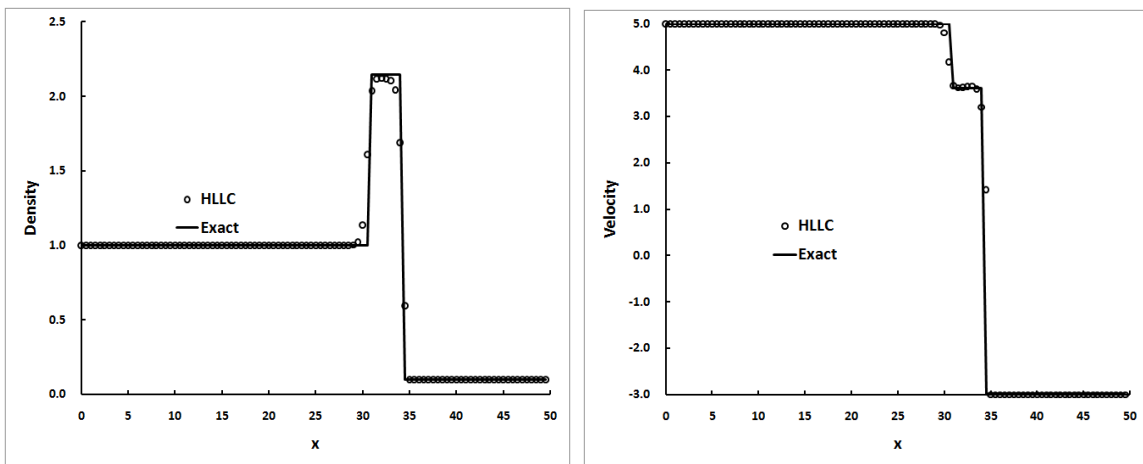


Fig. 7. The HLLC and the exact solutions of the density and velocity (test case 2)

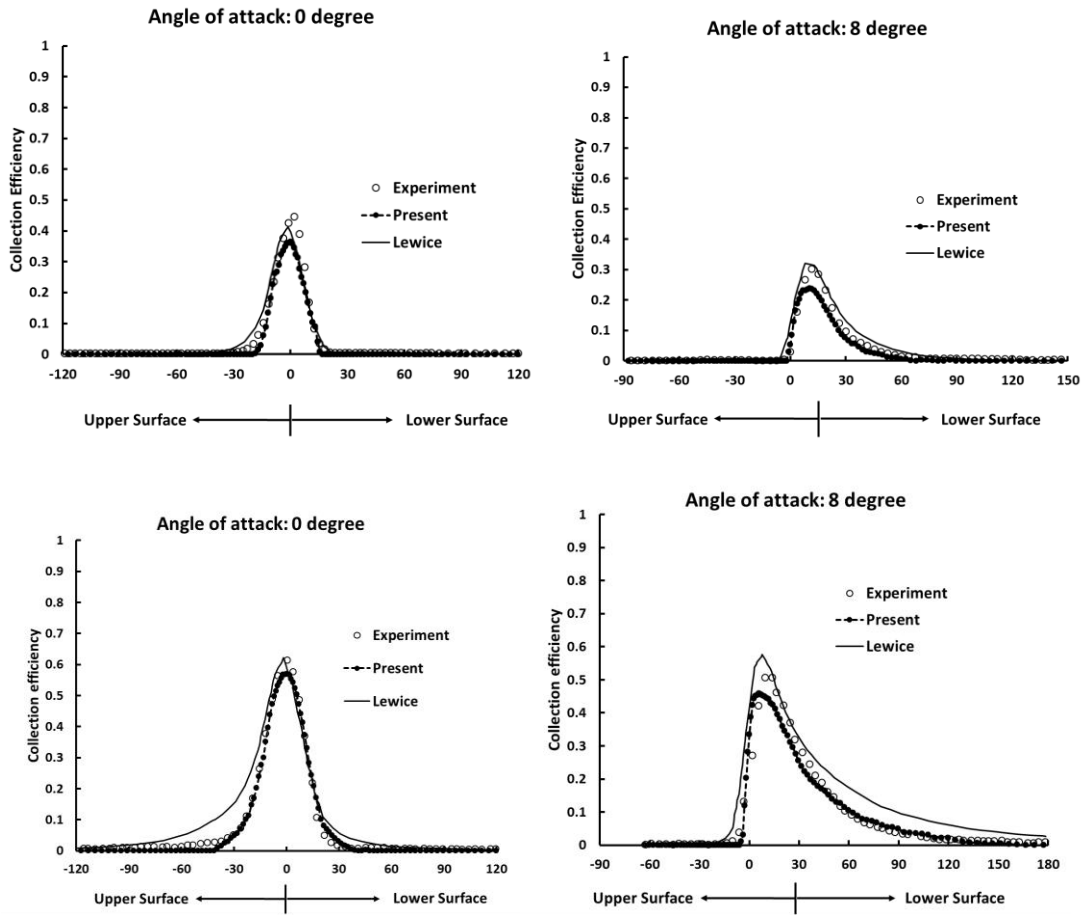


Fig. 8. The numerical and experimental results for the collection efficiencies (NACA 65₄₁₅ airfoil): (top) MVD 11.5 μm, LWC 0.05 g/m³; (bottom) MVD 21 μm, LWC 0.19 g/m³.

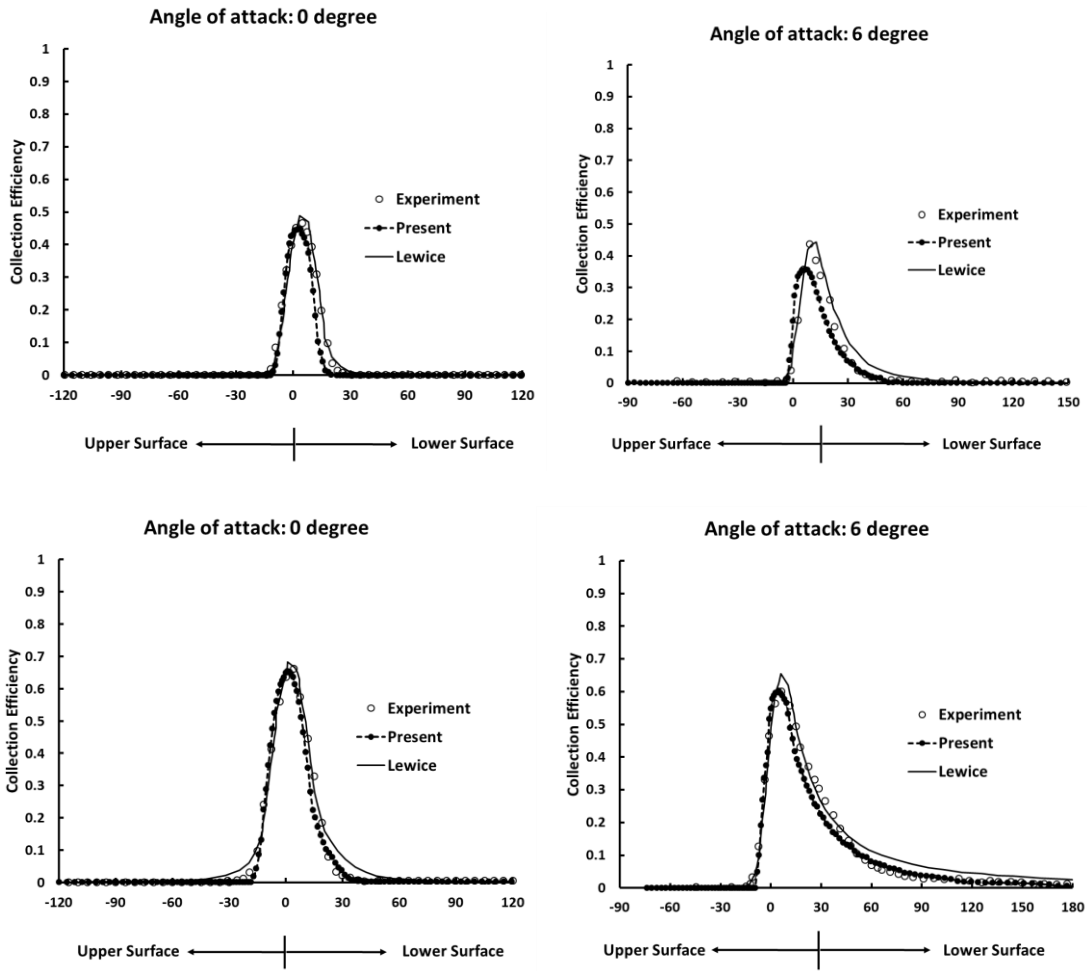


Fig. 9. The present and experimental results for the collection efficiencies (GLC 305 airfoil): (top) MVD $11.5\mu m$, LWC $0.05g/m^3$; (bottom) MVD $21\mu m$, LWC $0.19g/m^3$.

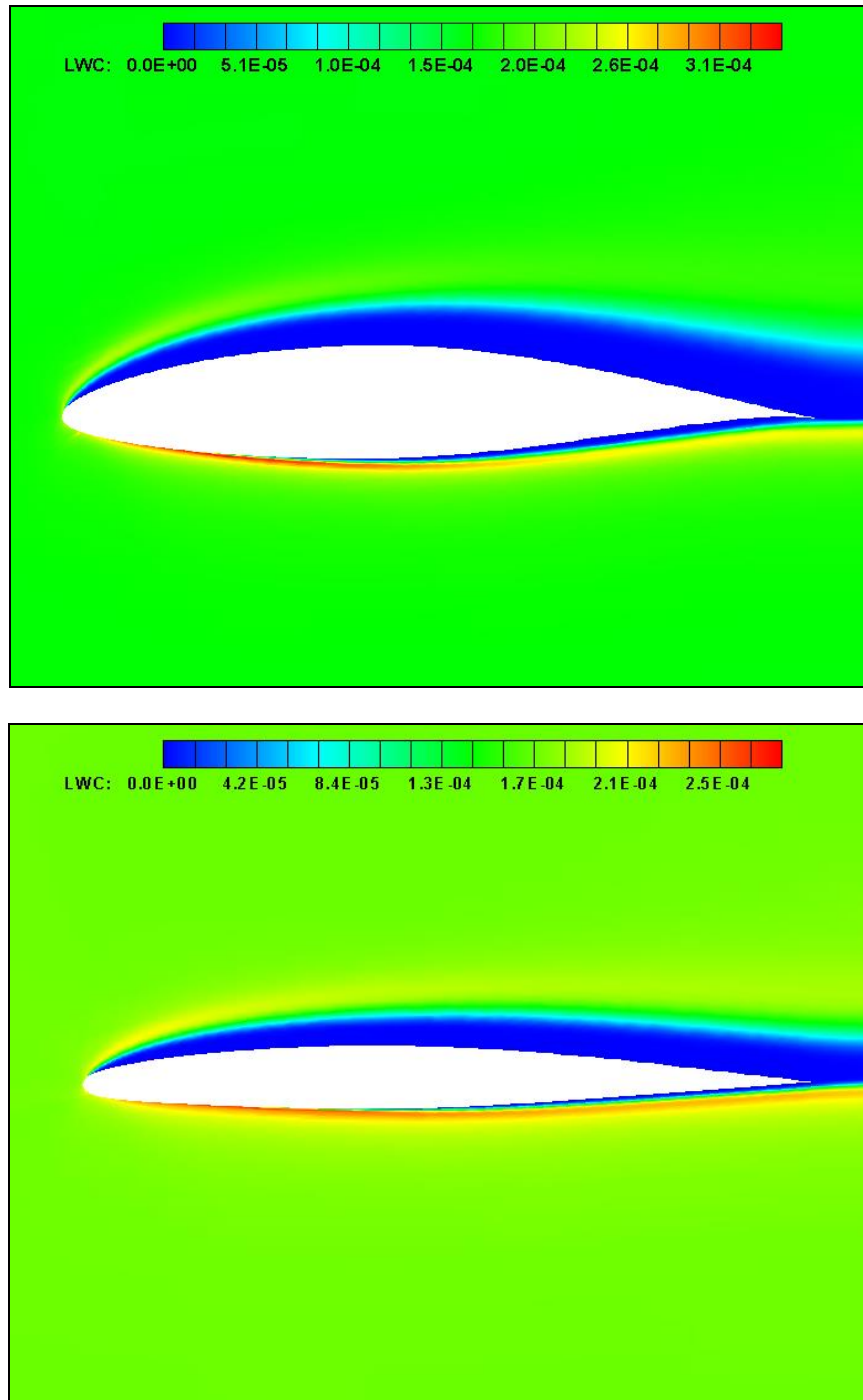


Fig. 10. The LWC distributions around NACA 65₄15 (top) and GLC 305 (bottom) (MVD 21 μ m, LWC 0.19g/m³).

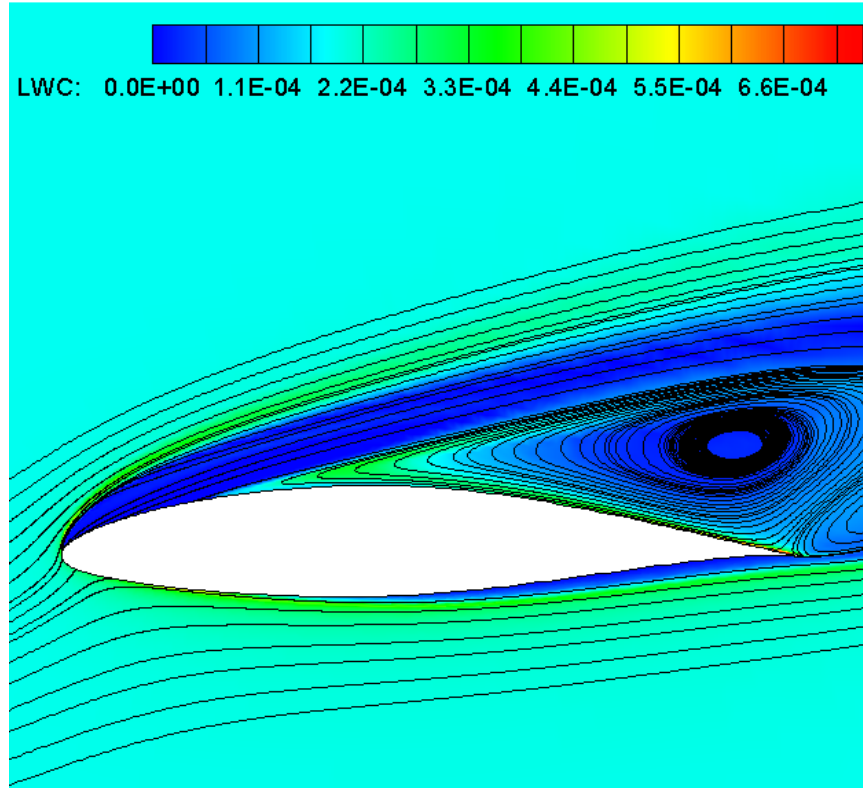


Fig. 11. Droplet trajectories and LWC distributions around NACA 65₂415 at high angle of attack (16 degrees, MVD 21 μ m, LWC 0.19g/m³).